Process-Induced Structures of Injection-Molded High-Density Polyethylene─Combining X-ray Scattering and Finite Element Modeling

N.B. When citing this work, cite the original published paper.

(article starts on next page)

Article

Process-Induced Structures of Injection-Molded High-Density Polyethylene—Combining X-ray Scattering and Finite Element Modeling

Linnea Björn, Elin Persson Jutemar, Renan Melhado Mazza, Eskil Andreasson, Fredrik Linell, Manuel Guizar-Sicairos, and Marianne Liebi*

Read Online

ACCESS | 📊 Metrics & More | 📖 Article Recommendations | 🆘 Supporting Information

ABSTRACT: The success of plastics heavily relies on fast melt processing methods used for large-scale industrial manufacturing, including injection molding. The hierarchical structure of the solid polymer depends on material selection combined with processing conditions, making mechanical properties of the injection molded part difficult to predict. Here we show how scanning small- and wide-angle X-ray scattering, birefringence microscopy, and polarized light optical microscopy can be combined with injection molding simulations to shed light on the correlation between the polymer morphology of high-density polyethylene and processing conditions. The scattering data revealed that the complex layered structure highly depends on the pressure during the holding phase of injection molding. Furthermore, we identified specific work of flow as a main parameter to capture the changes in morphology induced by varying the process settings. Overall, a good agreement was found between experimental data and the computational simulations, suggesting that computational simulations can be further used to predict the multiphase morphology of injection molded parts.

KEYWORDS: High Density Polyethylene, scanning WAXS, scanning SAXS, morphology, process settings, computational modeling, injection molding simulations
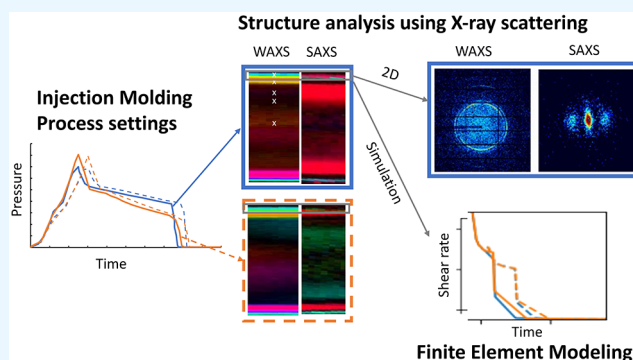
INTRODUCTION

Injection molding is a widely used processing technique in the polymer industry due to its ability to create identical plastic parts with complex shapes at a low price. Due to varying shear and cooling rates during processing, injection molding is known to create multiphase morphologies consisting of complex hierarchical semicrystalline structures, where different molecular orientation and crystallinity is found in different regions. Since the structures formed directly impact the mechanical properties of the injection molded part, understanding the correlation between processing conditions and resulting morphology is of essence. Historically, trial and error approaches have been used in industry to optimize the mechanical properties. For each new shape of a product that is tested, a new mold must be created. Furthermore, usually only one parameter is tested at a time, and since there are many parameters, such as pressure,[1,2] shear rate,[3] cooling rate,[4,5] and stress overshoot,[6,7] that affect the outcome, the trial and error method is both time-consuming and expensive. Being able to reliably predict the molecular structures formed during the processing is an important challenge. The development in industrial packaging strives to use virtual simulations instead of

trial-and-error testing to further improve material usage, as well as to test new shapes and materials. To link the mechanical performance and product performance with the processing conditions, a detailed material structure is needed.

Several studies have attempted to use computational simulations to predict the structures formed in various polymer materials during injection molding. Already in 1978, Tan et al. used mathematical models to predict the layered structure formed in injection-molded high density polyethylene (HDPE).[8] Patani et al. used simulations to calculate molecular orientation in injection-molded polystyrene,[9] and Zheng et al. used simulations to predict the flow-induced crystallization kinetics in isotactic polypropylene (iPP).[10] In addition, commercial software packages such as Moldflow have been used to simulate the injection molding process. A recent study
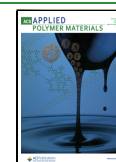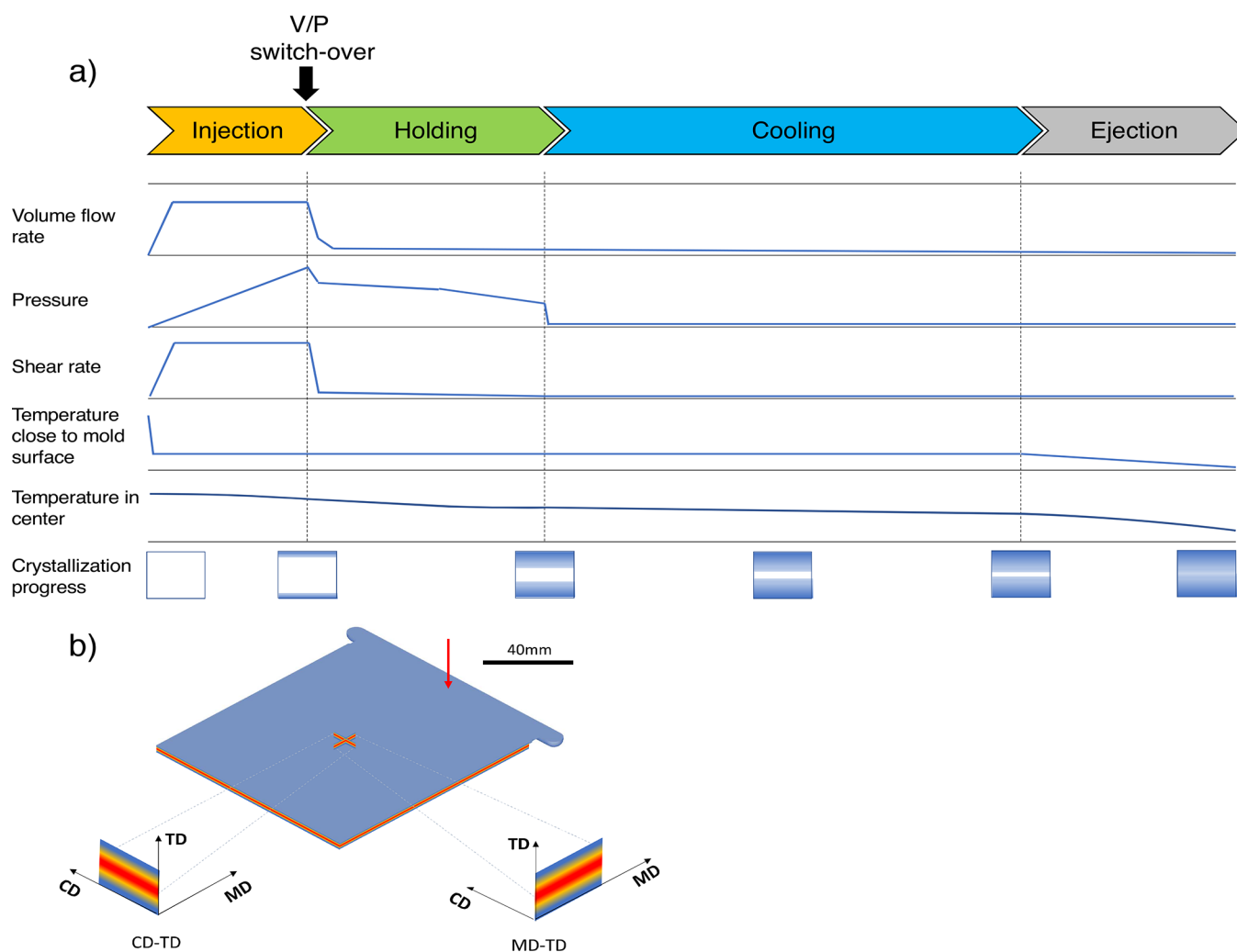
Figure 1. a) Schematic overview of an injection molding process. The volume flow rate is the volume of plastic melt passing through the point per time unit. The reported pressure is the pressure exerted by the reciprocal screw on the melted polymer. The shear rate is the maximum shear rate through the thickness. The temperature close to the mold surface is the temperature of the outer layer of the polymer. The temperature in the center is the temperature in the bulk of the melted polymer. b) Schematic representation of test plate following ISO 294-5 (thickness 0.6 mm), indicating position as well as machine direction (MD), cross direction (CD), and thickness direction (TD) for sample preparation of MD-TD plane and CD-TD plane cross sections. The red arrow indicates the injection point where the flow enters.

used Moldflow to study cavity modifications in injection-molded polyoxymethylene.[11]

In the above-mentioned studies, several different experimental techniques were used for validating the computational simulations, where the simulated data was compared to birefringence,[7] differential scanning calorimetry (DSC),[10] shrinkage measurements,[10] pressure profiles,[10] deflection,[11] and weight.[11] However, to improve simulations further, detailed information about the morphology formed during injection molding needs to be accounted for. One approach is to turn to small- and wide-angle X-ray scattering (SAXS and WAXS), which can be used to study hierarchical structures of semicrystalline polymers.[12−16] When semicrystalline polymers crystallize under quiescent conditions, the resulting morphology will be symmetrical spherulites,[17] whereas when crystallization occurs during high shear, the likely morphology is a so-called shish-kebab structure. The shish-kebab structure can have both twisted and untwisted lamellae, which can be differentiated by 2D WAXS and SAXS scattering data.[16,18] Recently, we have shown that scanning SAXS can be used to capture the multilayered morphology in low-density poly-

ethylene (LDPE) with a high resolution and that experimental data agrees with Finite Element Method (FEM) simulations of the injection molding process.[19] However, in this study, 2D WAXS data was not available, so the shish-kebab structures with twisted and untwisted lamellae could not be differentiated. Furthermore, the study did not investigate how varying the injection molding process settings influenced the results.

The aim of the current study is four-fold. The first part is combining high-resolution full azimuthal scanning SAXS and WAXS, polarized Light Optical Microscopy (LOM), and birefringence microscopy to reveal more details on the hierarchical structures formed in injection-molded HDPE. HDPE intrinsically has a higher degree of crystallinity compared to LDPE, so a more complex morphology is expected. The second part is to identify how process conditions influence the multiphase morphology, whereas the third and fourth parts are to use advanced FEM simulations to understand and eventually predict the structures observed in the experimental data. By showing how the complex morphology created during injection molding correlates with

computational simulations, the aim is to shed light on the link between process settings and resulting micro- and nanostructures, which can further be used to predict the mechanical performance of injection-molded polymer parts.

■ EXPERIMENTAL SECTION

Materials. HDPE with a Melt Flow Index (MFI) of 26 g/10 min (190 °C, 2.16 kg) and a density of 0.953 g/cm^3 was used throughout this work.

Injection Molding. An injection molding machine, i.e., an Arburg 470 800-70S hydraulic injection molding equipment, was used to produce test plates following ISO 294-5 (length 90 mm, width 80 mm, and thickness 0.6 mm), schematically represented in Figure 1. The plastic melt, with a temperature of 260 °C, was injected with a volume flow of 25 or 20 cm^3/s (as specified in Table 1) into a tool

Table 1. Process Settings Used during the Injection Molding Process

	Set injection volume flow (cm^3/s)	V/P switch-over point (%)	Holding pressure (bar)
High 85%	25	85	$1100 - 1\,s - 750$
High 99%	25	99	$1100 - 1\,s - 500$
Low 85%	20	85	$1100 - 1\,s - 750$
Low 99%	20	99	$1100 - 1\,s - 500$

with a temperature of 60 °C. The point at which the volume-controlled injection was switched to pressure-controlled holding is designated V/P switch-over (see Figure 1) and was varied between 85% and 99% cavity filling ratio, as specified in Table 1. The holding pressure for all settings was held for 1 s, decreasing linearly from the initial set and the end set holding pressure levels (presented in Table 1), which were chosen to obtain an even thickness of 0.6 mm over the plates. Holding pressure was followed by cooling for 11 s, the time chosen with margin to ensure sufficient solidification and crystallization under controlled cooling conditions before ejection. The actual volume flow rate was determined from the reciprocal screw position and the barrel diameter, while the actual pressure was calculated by multiplying the oil pressure behind the reciprocal screw and the intensification ratio. The fixed mold half was made from steel DIN 45 NiCrMo 16, while the moving mold half was made from the high-strength aluminum−zinc alloy AIZnMgCU 1,5. A schematic representation of the parameter evolution during the different phases of a typical injection molding process is presented in Figure 1. An in-depth description of each of the injection molding phases can be found in Supporting Information Section S1.

Sample Preparation for Measurements. From the injection-molded sample plates, cross sections through the thickness direction (TD) parallel to the machine direction (MD-TD) and its cross direction (CD-TD) were prepared as described in Figure 1. In addition, the cross section in the two 45° angles between CD and MD was cut, denoted as 45_1 and 45_2 (see Supporting Information Figure S1). The cross sections were cut to a thickness of 50 μm using a Leica RM2255 microtome from Triolab. Optical microscopy was performed on the same cross-section samples as birefringence microscopy, whereas for SAXS/WAXS measurements consecutive cuts from the same injection molding plate.

Birefringence Microscopy. Spatially resolved retardance and angle of the optical fast axis was measured with a birefringence imaging microscope (EXICOR MICROIMAGER, Hinds Instruments, Inc., OR). The optical elements consist of a linear polarizer at 0°, a photoelastic modulator (PEM) at 45°, a PEM at 0°, and a linear polarizer at 45°. Due to the high level of birefringence, phase unwrapping technology included in the Hinds software was used, which combined measurements from four stroboscopic light sources (LED, with wavelength 655, 615, 530, and 475 nm) to calculate the Mueller matrix components to retrieve quantitative values of the sample retardance and angle of the optical fast axis.[20,21] The samples

were measured with a 10× objective in front of a 2048 × 2048 pixel 12-bit CCD camera resulting in a pixel size of 1 μm and a field of view of 1 mm × 1 mm. The angle of the fast axis was color-coded using a color-wheel for easier interpretation and comparison with scattering data, where 0° corresponds to the cyan color and 90° corresponds to the red color.

Polarized Light Optical Microscopy. An Olympus BX51 optical microscope was used to analyze the polarizing properties of the samples. A 10× objective was used together with a 1.6× magnification changer for a total magnification of 16×. Specimens were mounted to an objective glass placed on the microscope stage. The polarizer, an Olympus AN-360, and analyzer, an Olympus U-POT, were cross-polarized and were for each specimen orientated to distinguish as clearly as possible the areas of different polarizing properties. Images were captured by using an Olympus dp73 digital camera mounted to the microscope.

Scanning SAXS and WAXS. Scanning SAXS and WAXS experiments were performed at the cSAXS (X12SA) beamline at the Paul Scherrer Institute (PSI, Switzerland). A Si(111) double crystal monochromator and X-ray energy of 12.4 keV was selected with the X-ray beam focused to 42 × 4 μm. In both SAXS and WAXS experimental setup, a Pilatus 2 M detector[22] was used. In the WAXS setup, the distance between the detector and the samples was 250 mm, a beamstop with a diameter of 800 μm was placed 25 mm behind the samples, and a pinhole of 1 mm diameter was placed 25 mm in front of the samples. In the SAXS setup, the detector was placed 2171 mm behind the samples, and in between the samples and the detector, a 2 m flight tube was placed to minimize air scattering and absorption. Cross sections of injection-molded samples were measured with an exposure time of 0.06 s and a step size of 40 μm × 10 μm in both SAXS and WAXS. In addition, higher resolution scans were performed for samples produced with the process settings High 85% and Low 99%, since these process settings were expected to give the largest differences in structural morphology. The step size for the high-resolution scans was 40 × 5 μm to match the size of the beam.

Each scattering pattern was analyzed for orientation and degree of orientation in specific q-ranges according to Bunk et al.[23] For analyzing the WAXS (110)- and (200)-peaks, q-regions of 14.3−16.3 nm^{-1} and 16.3−17.6 nm^{-1} were used, respectively. For analyzing the SAXS peak corresponding to the long distance between crystalline lamellae and amorphous regions, a q-region of 0.145−0.623 nm^{-1} was used. In this analysis approach, for each q-range, the scattering pattern was divided into 16 azimuthal segments, where the azimuthal intensity distribution was approximated with a cosine function. Examples of azimuthal intensities can be seen in Figure S3. The symmetric intensity in a$_0$ is defined as the average scattering over all azimuthal angles, the asymmetric intensity a$_1$ is defined as the amplitude of the cosine function, and the degree of orientation was defined as a$_1$/a$_0$. For representing the data, a combination plot of orientation and the asymmetric intensity was used, where both orientation and degree of anisotropy are encoded in the HSV-color. In such a plot, the orientation angle of the scattering is defined as the hue, and the asymmetric intensity is encoded in the value scale. Black areas in this representation correspond to isotropic scattering from nanostructures that do not show a preferred orientation. Radially integrated and Lorentz corrected data averaged over all azimuthal segments were used for performing peak fitting, both in SAXS and in WAXS. The power law decay before and after the peak was approximated by a negative exponential and subtracted from the data. The remaining signal was approximated with a Gaussian function, from which the peak position, width, and amplitude were obtained.

Finite Element Modeling. A commercial software Autodesk Moldflow 2019 was used to do the Finite Element Modeling. The finite element model consisted of fixed and moving tool halves, cooling lines, feed system, and a cavity (Figure S2). The plates and the cavity were modeled using 3D elements with a total of 5,033,414 tetrahedron-shaped elements. The cooling lines and the feed system were modeled using 1D elements with 780 beam elements. The injection point and the inlets of the cooling system were defined as boundary conditions, and the process settings used in the simulation

were the same as those used during the actual injection processes. The model uses the conservation equations of momentum, mass, and energy to characterize the flow field, with equations described in detail in Supporting Information Section S3.

The data coefficients used in the simulations are produced by fitting data from material characterization of the current HDPE grade of this study, by viscosity measurements, PVT measurements, and thermal conductivity measured in a capillary rheometer (Rheograph 75 from Göttfert), and specific heat measured by differential scanning calorimetry (DSC3+ from Mettler). The material viscosity coefficients are fitted using the Cross-WLF model[24] and the material specific volume is described as a function of the temperature and pressure by a 2-domain Tait PVT model as described in eq 1.

$$v(T, p) = v_0(T)\left[1 - C \ln\left(1 + \frac{p}{B(T)}\right)\right] + v_t(T, p) \quad (1)$$

Where:

- $v(T, p)$ is the specific volume at a given temperature and pressure;
- v_0 is the specific volume at zero pressure;
- T is the temperature, in K;
- p is the pressure, in Pa;
- C is a constant, 0.0894;
- B accounts for the pressure sensitivity of the material.

v_0, $B(T)$, and $v_t(T, p)$ are defined differently depending on if the temperature is above or below the volumetric transition temperature (T_t). In the upper temperature region ($T > T_t$), these were described by eqs 2, 3, and 4.

$$v_0 = b_{1m} + b_{2m}(T - b_5) \quad (2)$$

$$B(T) = b_{3m}e^{[-b_{4m}(T-b_5)]} \quad (3)$$

$$v_t(T, P) = 0 \quad (4)$$

Where b_{1m}, b_{2m}, b_{3m}, b_{4m} and b_5 are data-fitted coefficients, as defined in Table 2. In the lower temperature region ($T < T_t$), it is described by eqs 5, 6, and 7.

$$v_0 = b_{1s} + b_{2s}(T - b_5) \quad (5)$$

Table 2. Data Coefficients Used in the Simulation

Category	Symbol	Value	Units
Viscosity coefficients	n	0.2562	
	τ^*	1.40212×10^5	Pa
	D_1	1.31535×10^{18}	Pa·s
	D_2	153.15	K
	A_1	41.908	
	$A_2\sim$	51.6	K
2-domain tait PVT coefficients	b_5	407.15	K
	b_6	1.58×10^{-7}	K/Pa
	b_{1m}	1.186×10^{-3}	m³/kg
	b_{2m}	9.14×10^{-7}	m³/kg·K
	b_{3m}	1.09×10^8	Pa
	b_{4m}	5.374×10^{-3}	K⁻¹
	b_{1s}	1.023×10^{-3}	m³/kg
	b_{2s}	3.98×10^{-7}	m³/kg*K
	b_{3s}	3.66×10^8	Pa
	b_{4s}	1.80×10^{-6}	K⁻¹
	b_7	1.623×10^{-4}	m³/kg
	b_8	5.393×10^{-2}	K⁻¹
	b_9	1.20×10^{-8}	Pa⁻¹
Specific heat		2.596×10^3	J/kg·K
Thermal conductivity		2.32×10^{-1}	W/m·K

$$B(T) = b_{3s}e^{[-b_{4s}(T-b_5)]} \quad (6)$$

$$v_t(T, P) = b_7e^{[(b_8(T-b_5))-(b_9p)]} \quad (7)$$

Where b_{1s}, b_{2s}, b_{3s}, b_{4s}, b_5, b_7, b_8 and b_9 are data-fitted coefficients, defined in Table 2. The volumetric transition temperature (T_t) is defined by eq 8:

$$T_t(p) = b_5 + b_6p \quad (8)$$

Where b_5 and b_6 are data-fitted coefficients, defined in Table 2.

■ RESULTS AND DISCUSSION

The results section is divided into four parts. The first and second parts show experimental results from high-resolution scanning small- and wide-angle X-ray scattering combined with birefringence microscopy and light optical microscopy. The first part focuses on gaining insights into the complex hierarchical structures present in injection-molded HDPE, whereas the second part focuses on how process settings, such as injection speed and pressure, influence the multiphase morphology formed. The third and fourth parts show results from advanced FEM simulations, where the third part connects the computational simulations to the structures observed in the experimental data, and the fourth part evaluates the crystallization from an energy perspective.

Part 1: In-depth Investigation of the Multilayered Morphology. With the aim to collect detailed information on the multiphase anisotropic structures of injection-molded HDPE, cross sections of the through thickness layers were studied by means of scanning SAXS and scanning WAXS, for injection-molded HDPE. Results from one of the process settings (High 85%) are shown in detail, where the 2D SAXS and WAXS scattering pattern for 5 selected positions through the thickness, viewed from the two main directions, are presented in Figure 2 (normal to CD-TD and MD-TD planes as described in Figure 1), whereas a more comprehensive collection of data can be found in Figure S4 with 2D scattering patterns from 18 different positions through the thickness of plates viewed from four directions, respectively, with two additional directions being ±45° rotated from the other directions. Depending on the direction in which the measurement was performed, a contrast is achieved between the separate layers in the orientation analysis, as shown in Figure 2 (right). The WAXS (200) orientation was chosen as a sensitive indicator for different structures in the skin layers, as described in Figure S5, while the orientation of the SAXS signal of the lamellae spacing is more sensitive to identifying layers in the inner shear and bulk layers.

In the layer designated 1, very close to the surface toward the mold, the SAXS 2D pattern from both MD-TD and CD-TD showed a weak tendency for a vertical streak and a two-point pattern in the horizontal direction. Note that the orientation analysis performed to create the composed images in Figure 2 (right) will find the strongest orientation in the chosen q-range, where for MD-TD the horizontal two-point pattern dominates, whereas in CD-TD the vertical streak dominates mostly, apart from a thin line between layer 1 and 2 where the horizontal pattern appears stronger (turquoise line). These scattering patterns indicate the presence of a shish-kebab crystalline structure, where the streak represents the shish, and the two-point patterns represent the aligned lamellae in the kebabs, with a q-value representing the repeating distance between the lamellae. WAXS 2D scattering pattern in
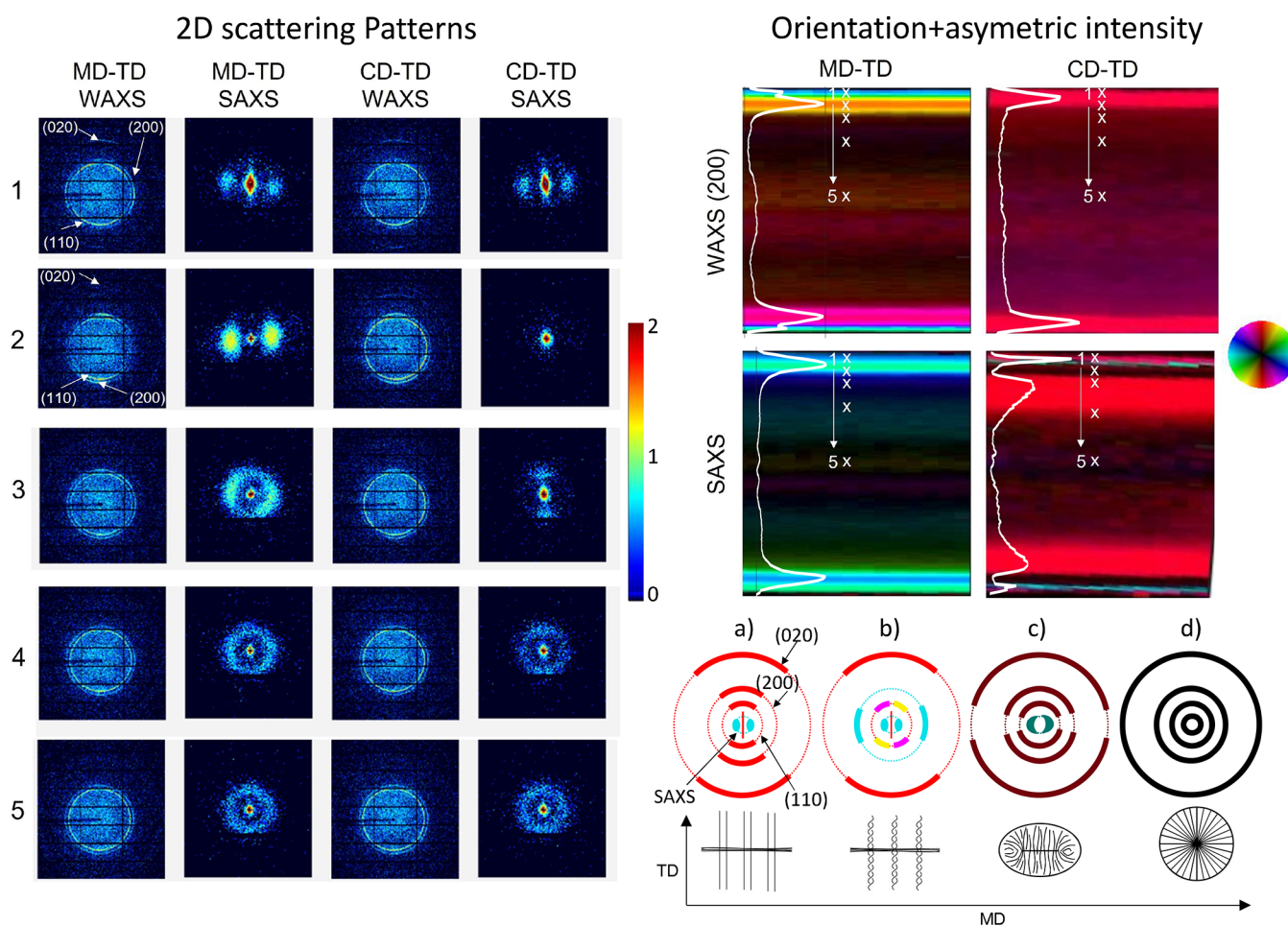
Figure 2. Scanning SAXS and WAXS 2D scattering patterns in five different positions (left) and orientation + asymmetric intensity (right top) of cross sections from samples produced with process settings High 85% as well as idealized scattering patterns of polyethylene in the MD-TD direction (right bottom). The idealized scattering patterns correspond from left to right with a) shish-kebab with untwisted lamellae, b) shish-kebab with twisted lamellae, c) elongated spherulites, and d) symmetrical spherulites. In the orientation + asymmetric intensity plots as well as in the idealized scattering patterns, the hue represents the scattering orientation, and the value shows the asymmetric intensity. The white profiles in the orientation + asymmetric intensity plots show the asymmetric intensity through the thickness. The crosses in the orientation + asymmetric intensity plots indicate the position of the 2D scattering patterns (1−5). The scattering patterns reveal shish-kebab with twisted lamellae (Keller−Machine Type I) in layer 1, shish-kebab with untwisted lamellae (Keller−Machine Type II) in layer 2, a highly oriented crystalline morphology in layer 3, elongated spherulites in layer 4, and symmetrical spherulites in layer 5.

MD-TD and less intensely in CD-TD further revealed the type of shish-kebab structure, with 4 maxima scattered as a cross along the vertical plane in the (110) crystal plane, two maxima along the horizontal plane in the (200) crystal plane, and two broad maxima along the vertical plane in the (020) crystal plane (see enlarged pattern in Figure S5). This is a typical WAXS scattering pattern for the structure known as Keller−Machin Type I structure, a shish-kebab with twisted lamellae.[18,25] In the layer designated 2, further into the sample, the vertical streak in SAXS disappeared, and only the 2D scattering pattern recorded in MD-TD showed a two-point pattern. Also, the WAXS 2D scattering pattern recorded in MD-TD changed, where the 4 maxima merged to 2 maxima along the vertical plane for the (110) crystal plane, while the two maxima of the (200) crystal plane shifted from the horizontal plane to the vertical plane (see enlarged pattern in Figure S5). The shift in the (200) signal could clearly be identified in the orientation and asymmetric intensity plot, changing color from blue to orange, i.e., an orientation angle of about 90° moving from layer 1 to 2. Despite the absence of the

streak, the crystal structure in this layer is believed to be the Keller−Machin Type II structure,[18,25] i.e., a shish-kebab with untwisted/regular lamellae. The reason for the absence of the two-point pattern in the SAXS 2D scattering pattern recorded in CD-TD is believed to arise from the untwisted/regular lamellae, not causing constructive interference scattering when viewed in the CD-TD plane, where the growth direction of the lamellae is facing the viewing angle.

In the layer designated 3, the orientation images in Figure 2 (right) indicate significantly reduced asymmetric intensity in the WAXS (200) diffraction but are characterized by a striking increase in asymmetry in the SAXS signal observed in CD-TD (red layer). The scattering from the lamellae spacing in the MD-TD SAXS pattern appears now as a ring, but with higher intensity in the horizontal plane, while in CD-TD, SAXS scattering with lower intensity is observed mainly in two maxima along the vertical plane. In WAXS, the scattering patterns in layer 3 showed significantly less orientation in all diffraction peaks than in layers 1 and 2. The 2D scattering pattern in WAXS and MD-TD SAXS would suggest the
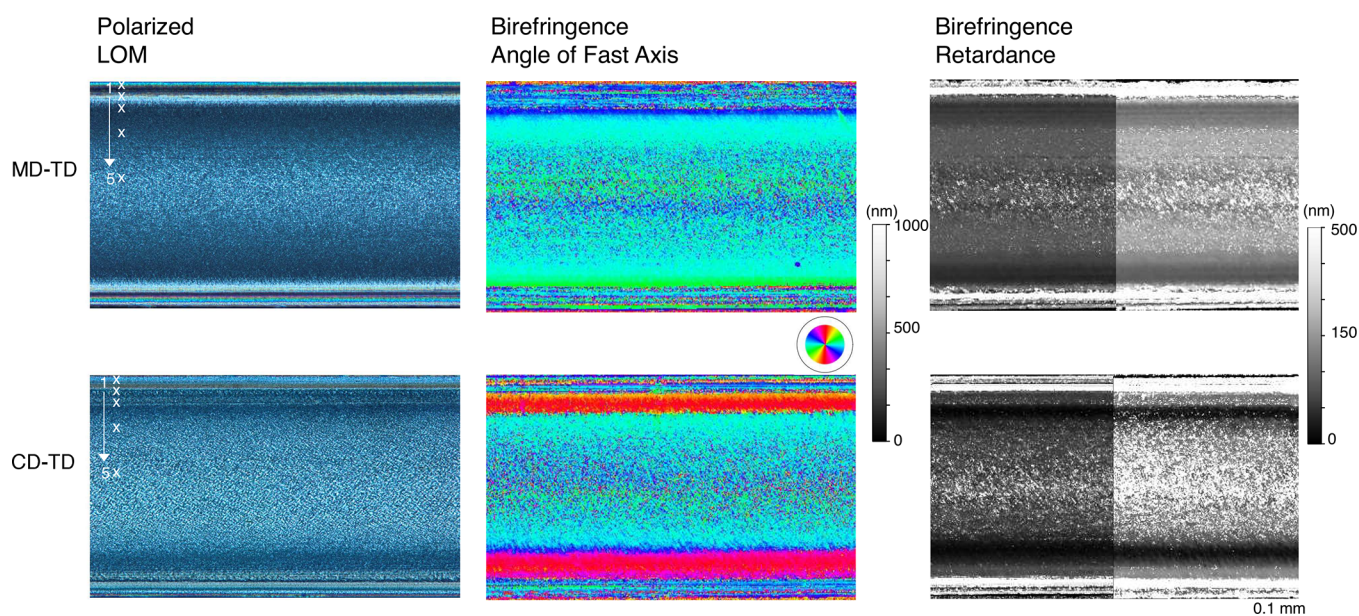
Figure 3. Birefringence microscopy angle of fast axis (left), retardance (middle) presented on two different scales, and polarized LOM microscopy images (right) on samples produced with process setting High 85% in the MD-TD plane (top) and CD-TD plane (bottom).

presence of highly elongated spherulites, with a structure described by Katti et al.[26] With such a structure, however, the 2D scattering pattern in SAXS CD-TD is expected to be more symmetrical over all the azimuthal angles,[19] whereas here we observe in the SAXS 2D scattering pattern in CD-TD a clear anisotropy of the scattering from the lamellae spacing in the vertical direction. This is also visible in the 45_1 direction (Figure S4), whereas the 45_2 direction in SAXS reveals even more complex orientation phenomena. Therefore, the structure present in this layer is most likely a highly oriented crystalline morphology, more complex in crystalline structure than an elongated spherulite oriented in the flow direction. While our results cannot be used to fully confirm the nature of this highly oriented crystalline morphology, we hypothesize that the orientation/geometry of this crystalline morphology is affected by both the direction of the flow in MD and the thermal gradient in TD.

The layer designated 4 is characterized by a significantly reduced asymmetric intensity in the CD-TD SAXS compared to layer 3 (Figure 2 right). The scattering pattern in SAXS reveals a ring from the lamellae spacing in both MD-TD and CD-TD, with somewhat higher intensity along the horizontal plane for MD-TD and along the vertical plane for CD-TD. In the WAXS scattering patterns, the scattering was rather isotropic, but with a tendency for higher scattering along the vertical plane in the MD-TD sample. These scattering patterns suggest the presence of somewhat elongated spherulites with a preferred orientation in the direction of flow in this layer. The transition from layer 4 to layer 5 appears rather gradual, mainly visible in the orientation images presented in Supporting Information and Figure S6.

In the layer designated 5, the appearance of the SAXS and WAXS patterns was isotropic, with no preferred orientation, suggesting the presence of symmetrical spherulites.

The layers in the second half (lower part) of the plate through the thickness presented scattering patterns reflecting those on the first half of the plate and will not be further discussed. SAXS and WAXS 2D scattering patterns from the second half can be found in Supporting Information and Figure S4.

In summary, Figure 2 shows that highly oriented shish-kebab layers can easily be identified by a significantly higher asymmetric intensity than the other layers, except for the SAXS CD-TD plane. The shift between shish-kebab with twisted lamellae and the shish-kebab with untwisted lamellae can easily be identified by reviewing the WAXS (200) signal in the MD-TD plane. The (200) WAXS signal shifts 90° in orientation angle upon the shift between twisted and untwisted lamellae, which is clearly seen in the transition of color in the WAXS MD orientation + asymmetric intensity plot. The presence of the highly oriented crystalline morphology can be identified by the higher asymmetric intensity in the SAXS CD-TD plane.

Polarized LOM and birefringence microscopy were performed on consecutive cross sections in both the MD-TD plane and CD-TD plane from plates produced with High 85% process settings (Figure 3). The layer identified as shish-kebab with twisted lamellae (Layer 1) appears as an outer lighter layer and an inner darker layer in MD-TD and an outer darker layer and an inner lighter layer in CD-TD with polarized LOM, while the layer identified as shish-kebab with untwisted lamellae (Layer 2) appears as a lighter layer in MD-TD, while being less defined in CD-TD. With birefringence microscopy, the two layers with shish-kebab could be distinguish from each other using the retardance, where the shish-kebab with twisted lamellae had a lower retardance compared to the shish-kebab with untwisted lamellae, in both MD-TD and CD-TD. The layer identified as highly oriented crystalline morphology (Layer 3) appears as a distinct layer in birefringence, with a very low retardance value as well as a slight shift in angle (presented in turquoise) in MD-TD and with an angle perpendicular (presented in red/pink) to the surrounding layers in CD-TD. With polarized LOM, however, this layer could only indicatively be identified as a darker layer in CD, while not discernible in MD-TD.

The layers identified as elongated spherulites and symmetrical spherulites (Layers 4 and 5) were more difficult to distinguish compared to the other layers. In birefringence microscopy images, there was a tendency toward a gradual change in both the retardance and the angle of the fast axis from the elongated spherulites to the symmetrical spherulites, more visible in MD-TD. With polarized LOM, the distinction between the layers was even more difficult, with the symmetrical spherulites giving rise to an indicatively lighter color in MD-TD, but not distinguishable at all in CD-TD.

The layered morphology found in birefringence and polarized LOM highly agrees with the scattering data from scanning SAXS/WAXS, in terms of both layer distribution and orientation seen by the angle of the fast axis in birefringence. This is of high industrial interest because, first, birefringence microscopy and polarized LOM are more readily available and can be used to further investigate the changes in morphology of semicrystalline polymers with varying processing conditions, and second, it provides higher spatial resolution compared to scanning SAXS/WAXS and can more easily be used to quantify the thickness and distribution of layers. Scanning SAXS/WAXS on the other hand reveals the nanostructural features and diffraction pattern that can be used as fingerprints to identify the different morphologies. Therefore, scattering techniques and optical microscopy complement each other.

The peak position and peak width at half-maximum were obtained from peak fitting of WAXS and SAXS in MD-TD plane and are presented in Supporting Information Section S4 and Figure S8. d-spacing in WAXS ranged between 0.4125 to 0.4132 nm, with the shish-kebab with twisted lamellae (layer 1) having the largest d-spacing. We hypothesize that the twisting of the lamellae introduces strain into the crystal unit cell, resulting in a longer d-spacing. In the SAXS regime, the main scattering peak corresponds to the distance between crystalline lamellae, i.e., the distance of one crystalline and one amorphous layer. The largest distance between crystalline lamellae was found in the layer consisting of shish-kebab with untwisted lamellae. The broadest peak width in both SAXS and WAXS was identified in the layer consisting of highly oriented crystalline structure. In the SAXS regime, this indicates that we have a high variation in the lamellae spacing. In the WAXS regime, we hypothesize that the broadening of the peak could be caused by smaller crystallite sizes, strains within the crystallite structure, or a combination of the two.

Part 2: Investigating the Influence of Process Settings. In the second part of the study, injection-molded samples produced with varying process settings were investigated using the same approach to further link process conditions with structural morphology. The orientation analyses from the WAXS (200) MD-TD and SAXS CD-TD were chosen based on part 1, which revealed that the different layers can be identified best in this combination.

The samples were produced using four different process settings by adjusting two process parameters, i.e., injection speed and V/P switch-over point, as defined in Table 1. The parameter injection speed was chosen to vary the injection shear rates, while the parameter V/P switch-over was chosen to vary the injection time and holding pressure level. A schematic representation of the phases and parameters during the injection molding process is shown in Figure 1, and a more in-depth description is presented in Supporting Information, Section S1. The measured volume flow rate during the injection molding cycle for the four different process settings is

presented in Figure 4a. The flow rates in the injection phase were approximately 22 cm³/s for the process settings with high
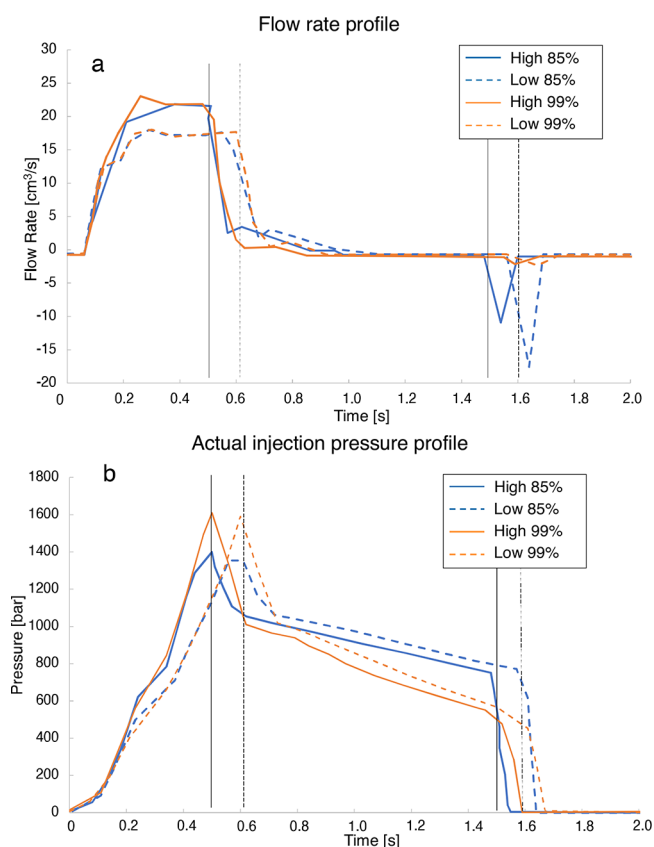

Figure 4. Flow rate (a) and pressure (b) as a function of time, as measured during the injection molding process. The positions of the V/P switch-over point and transition from holding to cooling phase, respectively, are indicated by full lines (high flow rate) and dotted lines (low flow rate).

injection speed, and the measured flow rate of approximately 17 cm³/s for the process settings with low injection speed. Expectedly, a higher level of flow rate in the initial parts of the hold pressure phase was identified for the settings using 85% V/P switch-over point than for 99%, since not only does shrinkage need to be compensated for but also filling the cavity from 85% to 100%. The apparent drop in flow rate registered at about 1.5 s occurred at the point when the hold pressure was released and the cooling phase started and could most likely be explained by a slight reversing movement by the reciprocal screw at the release of the hold pressure.

The measured pressures during the injection molding cycle for the four different process settings are presented in Figure 4b. Notably, the injection pressure for the process settings using a 99% V/P switch-over point ended at a higher level than for 85%, which can be explained by the higher filling ratio of the mold at the end of the injection phase, resulting in a higher pressure needed to keep the constant flow rate. Notably, as defined in Table 1, the hold pressure level for the settings using an 85% V/P switch-over point was higher than the settings using 99%, since it was required to obtain plates with an even thickness of 0.6 mm when filling of the mold continued after the initiation of the hold pressure phase, as compared with the 99% settings, where the mold was virtually filled already at the V/P switch-over point.
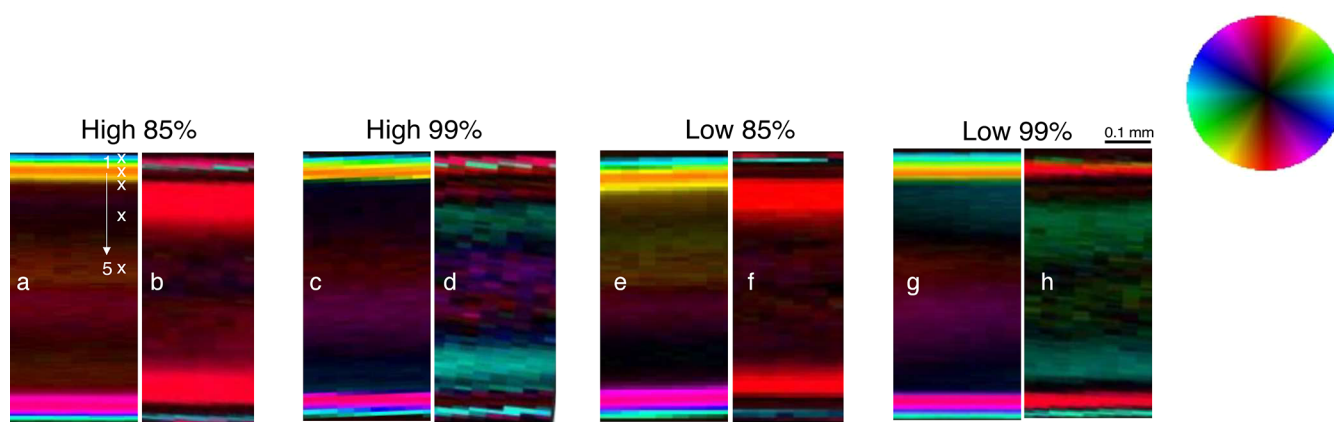
Figure 5. Scanning SAXS and WAXS (200) orientation + asymmetric intensity through the thickness of cross sections from samples produced with varying process settings. Cross sections to the left of each pair (a, c, e, and g) represent WAXS (200) MD-TD, and cross sections to the right of each pair (b, d, f, and h) represent SAXS CD-TD.

To investigate how the V/P switch-over point and injection speed influenced the multilayered structure, cross sections of the through thickness layers were studied by means of scanning SAXS and scanning WAXS, viewed in 2 different directions for samples produced with the four different process settings. Plots representing orientation and asymmetric intensity for the (200) crystal plane WAXS scattering peak in MD-TD and SAXS main scattering peak in CD-TD are presented in Figure 5. The asymmetric intensity profiles are also shown as 1D plots in Supporting Information and in Figure S7. The orientation angle and asymmetric intensity of the shish-kebab layers (previously described as layers 1 and 2) showed similar characteristics for all four process settings, but there was an indication of thicker shish-kebab with untwisted lamellae (layer 2) for the settings using a V/P switch-over point of Low 85% than with 99%, seen with the yellow/orange (upper) and purple (lower) color in the WAXS (200) asymmetric intensity in MD-TD (Figure 5a and e in comparison with Figure 5c and g). Another visible difference between process settings was the presence of the thick layer of highly oriented crystalline morphology, described previously in layer 3, seen as red layers in the SAXS CD-TD, in the samples produced with 85% V/P switch-over point (Figure 5b and f), while not being present at all in the samples produced with 99% switch-over point (Figure 5d and h). The thickness of this highly oriented crystalline morphology layer was different in the upper and lower parts of the sample, which most likely originated from the different mold materials in the two mold halves, giving rise to different cooling rates on the two sides of the cavity. The samples produced with 99% V/P switch-over point instead showed in this region an outer layer with significantly lower intensity in SAXS CD-TD but same orientation (Figure 5d and h), indicated by the red color. The same layering type was observed for the low and high flow settings with a slightly increased degree of orientation in the high flow setting (higher color saturation in Figure 5d compared to that in Figure 5h).

The spatially resolved d-spacing obtained from the peak fitting of Lorentz corrected SAXS radially integrated curves for different process settings is presented in Figure 6. The main scattering peak represents the lamellae spacing, i.e., the repeating distance of d_{ac}, which is the sum of the thickness of the lamellae, d_c, and the surrounding amorphous layer, d_a, i.e., the repeating distance between kebabs for the shish-kebab morphology. Comparing the samples produced with varying
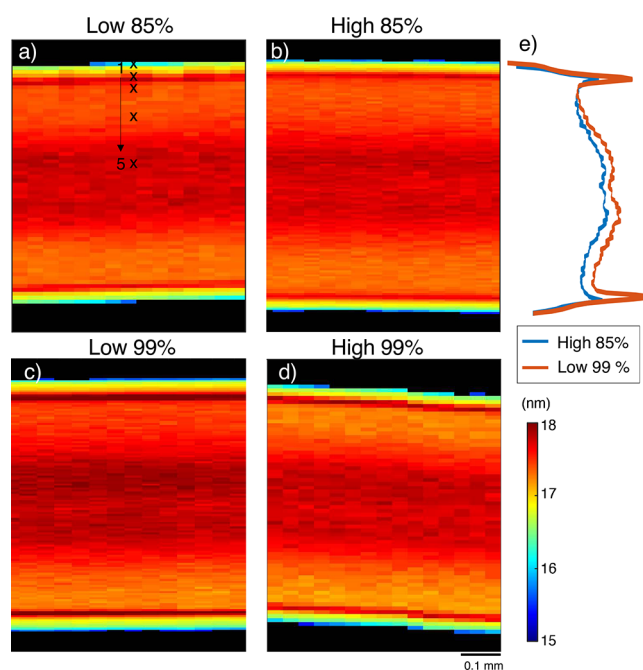

Figure 6. Peak fitting from SAXS data in MD-TD plane of a sample produced with process setting High 85% (a), Low 85% (b), High 99% (c), and Low 99% (d), where the d-spacing from the 2π/peak position is shown. Note that High 85% and Low 99% are measured with higher resolution. Figure 6e shows how the peak position that was found through peak fitting varied through the thickness for the high-resolution measurements.

process settings, more specifically when comparing the d-spacing profiles through the thickness of the two high-resolution cross sections (High 85% and Low 99%), it can be observed that layer 2, consisting of shish-kebab with untwisted lamellae, as well as the bulk region (layer 5) present significantly larger lamellae spacing for low injection speed compared with high setting speed, as well as larger lamellae spacing for 99% V/P switch-over point than for 85% V/P-switch-over point.

Birefringence microscopy and polarized LOM was performed on the cross sections next to those investigated with SAXS and WAXS for all four process settings. Images from those are presented and discussed in Supporting Information
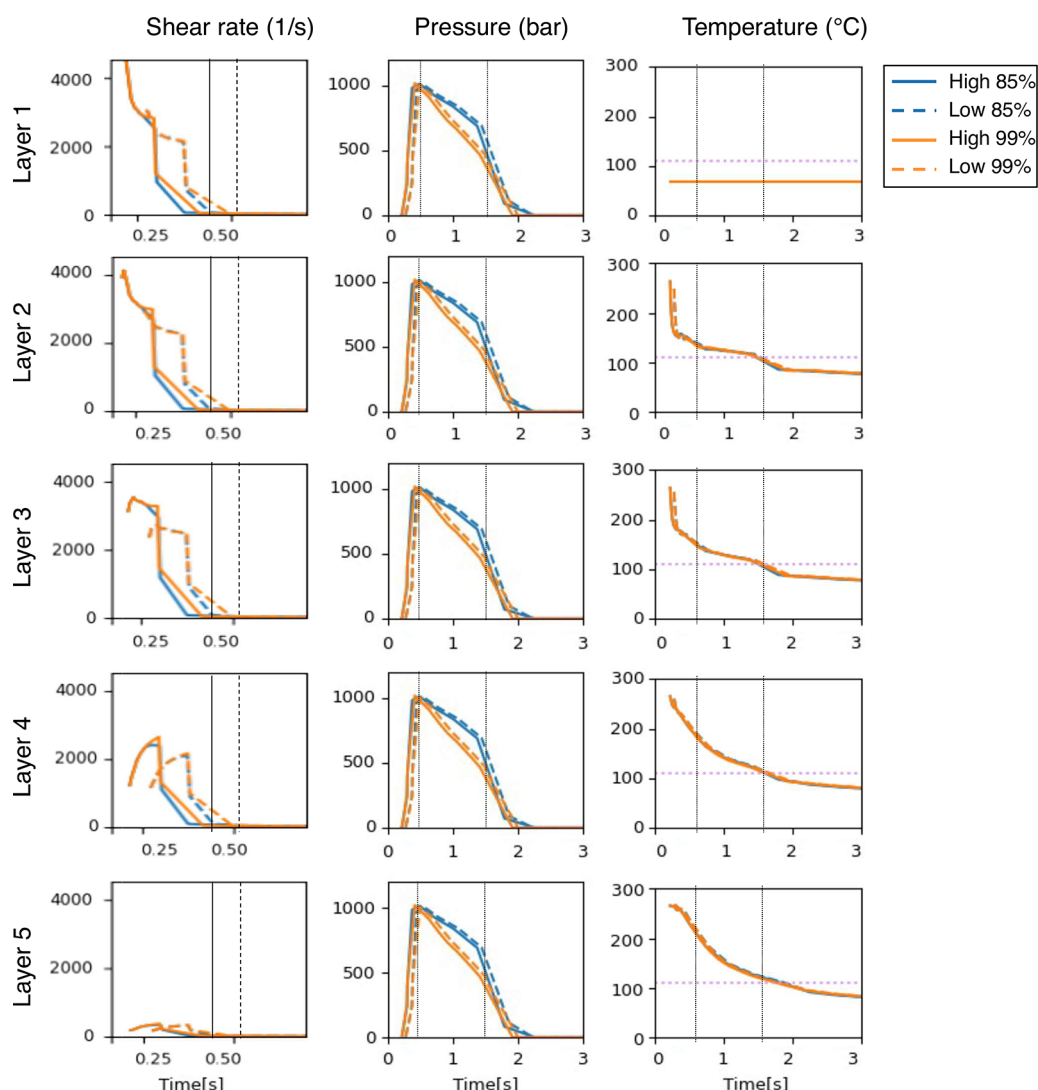
Figure 7. Selected results from finite element simulations: shear rate (left), pressure (center), and temperature (right), in five different layers through the thickness, where layers 1 to 5 represent different depth from the mold wall, i.e., 0.00, 0.03, 0.06, 0.15, and 0.27 mm. These depths were chosen to represent the same layers reported in Figure 2. Note that the x-axis, i.e., the time, was chosen differently for the three parameters. Horizontal purple dotted lines represent the quiescent crystallization temperature of 117 °C. The vertical black lines indicate the transition between injection phase and the hold phase (∼0.5 s) and the transition between the hold phase and cooling phase (∼1.5 s).

and Figure S9. The results agreed with the observations from scanning SAXS/WAXS, and the results can be used as a complement to the scanning SAXS/WAXS measurements.

Part 3: Connecting Scattering Data to Computational Simulations. To further correlate the multilayered structure created during injection molding to processing conditions, finite element simulations were used, where some selected results from finite element simulations are presented in Figure 7. The results are presented in a collection of graphs, where the columns report the shear rate in the flow direction, pressure, and temperature, respectively. The time evolution of shear rate, pressure, and temperature is shown within the five different layers through the thickness identified in the SAXS data.

Layers 1 and 2 present similar results for pressure and shear rate, whereas in the temperature history for layer 1, being closest to the cold mold wall, the cooling rate is extremely high, resulting in temperatures below the quiescent crystallization temperature (117 °C, as indicated with a purple horizontal pointed line), almost instantaneously. Thus, crystallization is expected to occur in the flow front and may therefore occur

under the influence of the fountain flow and with limited relaxation time during cooling.[9,27,28] In layer 2, the time at which the temperature becomes lower than the quiescent crystallization was reached at about 1.3 s, where the shear rate dropped significantly. However, flow-induced crystallization occurs at higher temperature,[29] and more specifically, the creation of shish precursors occurs well above the quiescent crystallization temperature.[30−32] Therefore, it is expected that most of the flow-induced crystallization was initiated already during the injection phase, followed by crystallization of the kebabs at a lower temperature in the holding phase. With a longer time in the melt state above the transition temperature, it is expected to give better conditions for the creation of shish-kebab crystallization morphology. Further, with longer time at high shear rate, while still under high cooling, the conditions are more favorable for creation of higher amounts of shish, resulting in more beneficial conditions to form untwisted lamellae as compared with the twisted lamella[32] in layer 1.

The simulation shows that the shear rate has dropped in the holding phase and occurs under significantly different pressure

when comparing the samples with 99% and 85% V/P switch-over, as expected according to the process settings shown in Table 1. It has previously been shown that an increased pressure during processing is linked with a higher formation of the shish-kebab morphology.[33] Thus, we hypothesize that the pressure history is the main contributor for the thicker layer 2 in samples produced with the 85% V/P switch-over point in comparison with the 99% V/P switch-over point, as shown in orientation and asymmetric intensity in SAXS and WAXS (Figure 5).

Furthermore, the simulations show that the shear rate is lower and the time duration under shear is longer for a low injection speed in comparison with a high speed (Figure 7). This could possibly give fewer nucleation sites for kebabs on the shish precursors, which could explain the longer d-spacing between the kebabs for samples produced with low injection speed in comparison with high speed, as shown in Figure 6. d-spacing was also shown to be longer for the 99% V/P switchover point than with 85%. The kebabs formed under lower pressure, and hence lower temperature when using the 99% V/P switch-over point could be a possible explanation for the longer d-spacing between the kebabs, as shown in Figure 6.

In layer 3, cooling occurred more slowly, and the quiescent crystallization temperature was reached at a later stage compared to layers 1 and 2. When the quiescent crystallization temperature was reached at about 1.5 s, the shear rate dropped significantly. Since this layer still presents a high shear (similar to layers 1 and 2) during the injection phase, one can expect a high orientation of the melt prior to crystallization, which could increase the likelihood of creating fibrillar nucleation cores for spherulites, which consequently could result in more anisotropic crystals, i.e., highly oriented crystalline morphologies. The pressure was significantly higher for the settings with a V/P switch-over point of 85% in comparison with 99%, and crystallization was therefore expected to occur under higher pressure for the samples produced with the 85% switch-over point. This result agrees with the differences identified in SAXS/WAXS (Figure 6) and polarized LOM (Figure S9), where the highly oriented crystalline morphology was present only when using the 85% V/P switch-over point.

In layer 4, the shear rates were further decreased in comparison with those of layers 1−3. Also, the cooling speed was more uniform as opposed to the layers closer to the mold wall. Similar to layer 3, the quiescent crystallization temperature was reached after about 1.5 s but proceeded by a history of longer time under higher temperature compared to layer 3, which enabled the polymer molecules to relax. Thereby, the probability for creating fibrillar nucleation cores is decreased, which consequently would result in a less anisotropic morphology than in layer 3.

In layer 5, the time when the quiescent crystallization temperature was reached was after 1.8 s, with low or almost no history of shear rate, indicating crystallization under nearly quiescent conditions at 117 °C, which occurred after the pressure approached ambient. Under these circumstances, no shear, slow cooling, and low pressure, nearly symmetrical spherulites were expected to develop.

As concluded in previous paragraphs, the difference identified between layers cannot be described in a unique parameter such as only shear or cooling rate, but indeed, the history of several conditions needs to be observed, as exemplified in the summary table reported in Supporting Information (Table S1).

Part 4: Evaluation of the Crystallization from an Energy Perspective. Previous work from experimental observations reported by Mykhaylyk et al.[34,35] have shown that there are two factors responsible for the formation of shish-kebab morphology by flow-induced crystallization: the critical shear rate $\dot{\gamma}$, which has been reported extensively over the years,[30,36] and a critical amount of specific work, w_c applied. The critical shear rate is estimated by $\dot{\gamma} \approx 1/\lambda_R$, where λ_R is the longest Rouse relaxation time of the molecules, proportional to the square of the molecular weight.

With the presence of shish-kebab morphology in the outer layers of the samples produced with all four process settings, the critical shear rate is obviously exceeded independent of the injection speed and V/P switch-over point. The higher degree of orientation and the thicker layer of shish-kebab with untwisted lamellae for the samples produced with 85% V/P switch-over point must consequently originate from another factor, i.e., the specific work. The specific work, w, is given by the integral of the product of the viscosity, η, and the square root of the strain rate during the shearing time, t_s, as given by the hypothesis and equation stated by Janeschitz-Kriegl et al.[37]

$$w = \int_0^{t_s} \eta[\dot{\gamma}(t)]\dot{\gamma}^2(t)\mathrm{d}t \tag{9}$$

The specific work combines all of the factors included in the simulation graphs reported in Figure 7. The shear rate $\dot{\gamma}$ is a factor as is, as well as being a contributing factor to viscosity η. Similarly, temperature is a factor affecting viscosity η. Pressure is a factor affecting the equilibrium melting temperature T_m°, and hence affects the temperature range in which crystallization occurs, which consequently affects the viscosity as the presence and amounts of crystals affect the viscosity.

While the majority of previous studies have been performed under isothermal conditions, and under constant shear rates, modeling of the specific work under the highly nonisothermal and varying shear rate conditions prevalent during the injection molding process is significantly less studied, reported by Liparoti et al.,[38] Pantani et al.,[39] and Du et al.[40]

To account for the highly nonisothermal and nonconstant conditions of the injection molding process, an alternative approach is employed to calculate the specific work, by limiting the integration time interval to the time when the equilibrium melting temperature T_m° is reached and the time at which 117 °C is reached, i.e., in the temperature interval where crystallization, flow-induced or quiescent, could occur. The equilibrium melting temperature is pressure-dependent, and can be expressed as a polynomial function, as reported by Fulchiron et al.[41] following:

$$T_m^\circ(p) = T_m^\circ(0) + a_1 p + a_2 p^2 \tag{10}$$

The factors T_m°, a_1, and a_2 were obtained from linear regression analysis from pressure−volume−temperature (PVT) data and were determined to be 135.6, 0.069, and 0.051, respectively for the polymer used in this study. The pressure, shear rate in the flow direction, and viscosity were obtained from the finite element analysis. The calculated specific work is presented in Figure 8 with clear differences between the V/P switch-over points. In the ranges 0−0.1 and 0.9−1.0 nominal thickness, corresponding to layers 1 and 2 with shish-kebab morphology, the specific work was significantly higher for the samples with 85% V/P switch-over point than in those with 99% V/P switch-over point. The higher specific work could explain the
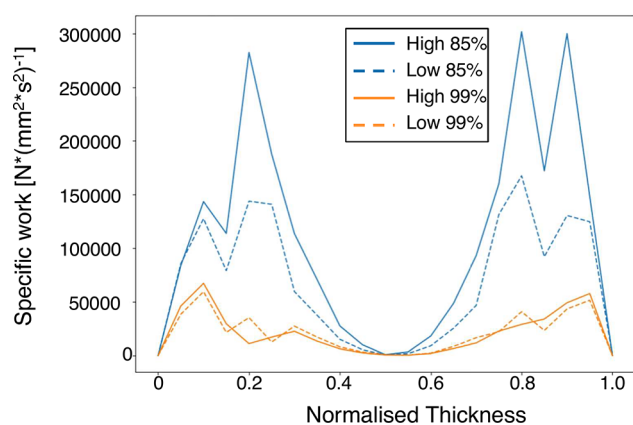
Figure 8. Calculated specific work as a function of the nominal thickness for four different process settings, i.e., high and low flow rate and V/P switch over at 85% and 99%, respectively.

difference in layer thickness of shish-kebab identified by polarized LOM and the different asymmetric intensity from SAXS/WAXS. The highest levels of specific work were identified for High 85% and Low 85% in the approximate ranges of the thickness where highly oriented crystalline morphologies were identified by SAXS/WAXS for the samples produced with these process settings. The maximum shear rates in layers 2 and 3, as presented in Figure 7, were on a rather similar level, while only shish-kebab structure was identified in layer 2. However, in layer 3, the highest shear rates occurred during the time when the temperature was higher than that at the corresponding shear rates in layer 2. At this higher temperature, despite a shear rate likely above the critical level, temperature was likely too high for oriented nuclei to form and for shish to grow. However, the high level of specific work in layer 3 using the process setting with 85% V/P switch-over resulted in a highly oriented crystalline morphology with significantly higher anisotropy than the elongated spherulites in layer 4.

CONCLUSION

The first part of this study showed how high-resolution full azimuthal scanning SAXS and WAXS can be used to reveal a complex multilayered structure in injection-molded HDPE. Due to the microfocused X-ray beam, high resolution was achieved, giving more in-depth details on the layered structure identifying 5 main layers. Highly oriented shish-kebab structures could easily be identified, where the WAXS signal was used to differentiate between twisted and untwisted lamellae in shish-kebab structures. Comparing the scattering data with polarized LOM and birefringence microscopy measurements, the distribution of the morphology was confirmed, demonstrating that once the structure of the layers is understood by X-ray scattering, easy accessible visible light microscopy techniques can be used to compare between more variation of process settings.

The second part of this study investigated how the V/P switch-over point and injection speed influenced the layered morphology. The scattering data revealed similar degrees of orientation profiles through the thickness for samples produced with the same V/P switch-over point. In samples produced with 85% V/P switch-over point a thick layer of highly oriented crystalline morphology was identified, which could not be identified in samples produced with 99% switch-

over point. This agreed with experimental data from both birefringence microscopy and polarized LOM, confirming that the V/P switch-over point has a large influence on morphology, larger than the flow rate. Peak fitting of the scanning SAXS data further revealed that the low injection speed results in shish-kebab with untwisted lamellae (layer 2) with a significantly larger lamellae spacing compared to the high injection speed and 85% V/P switch-over point.

The third part of the study used computational simulations to correlate process conditions to the resulting polymer morphologies by evaluating shear rate, pressure, and temperature through the thickness of the injection-molded plate. The formation of shish-kebab structures was associated with high shear rates, and it was established that when the polymer was subjected to high shear rates for a longer time, shish-kebab with untwisted lamellae is more likely to be formed compared to shish-kebab with twisted lamellae. However, by only looking at the simulated shear rate, pressure, and temperature, the conditions that drive the different morphologies seem to be more complex than just evaluating the shear history.

In the fourth part, in order to better understand what drives the morphology after the different process settings, the specific work was calculated for the different process settings, combining several factors, i.e., shear rate, time, temperature, and pressure, which resulted in high agreement with experimental data. In particular, the highest levels of specific work were identified for High 85% and Low 85% in the approximate ranges of the thickness where highly oriented crystalline morphology was identified by SAXS/WAXS.

In summary, this study shows that experimental data from high-resolution scanning SAXS/WAXS agree well with FEM simulations, proving that computational simulations can be used to predict hierarchical anisotropic structures of the polymer during injection molding. The holding pressure applied introduced a significant influence in the morphology, detectable by both experiments and specific works calculations. Thereby, this study brings us one step closer to being able to reliably predict the polymer microstructures after injection molding and further predict material properties of injection molded parts.

ASSOCIATED CONTENT

ⓈI Supporting Information

The Supporting Information is available free of charge at https://pubs.acs.org/doi/10.1021/acsapm.4c00581.

Description of each of the injection molding phases; Sample preparation of two additional cutting planes; Extended method for finite element model (figure of the model system; equations of momentum, mass and energy); Extended SAXS/WAXS analysis of the multi-layered morphology (Azimuthal integrated intensities of SAXS and WAXS data; scanning SAXS and WAXS + 2D scattering patterns from 18 positions through the thickness; 2D scattering patterns of shish-kebab with twisted lamellae and shish-kebab with untwisted lamellae; Scanning SAXS and WAXS orientation in MD-TD plane; Asymmetric intensity profiles in along the thickness direction (TD) for HDPE produced with different process settings; Peak fitting results of (100) peak in WAXS and lamellae spacing peak in SAXS) Extended analysis using birefringence microscopy and LOM (Birefringence and LOM through the thickness

from samples prepared with varying process settings.); Conclusion overview (PDF)

■ AUTHOR INFORMATION

Corresponding Author

    Marianne Liebi − *Department of Physics and FibRe-Centre for Lignocellulose-based Thermoplastics, Department of Chemistry and Chemical Engineering, Chalmers University of Technology, Gothenburg 412 96, Sweden; Paul Scherrer Institute, Villigen 5232, Switzerland; Ecole Polytechnique Fédérale de Lausanne (EPFL), Lausanne 1015, Switzerland;* orcid.org/0000-0002-5403-0593;
    Email: Marianne.liebi@psi.ch

Authors

    Linnea Björn − *Department of Physics and FibRe-Centre for Lignocellulose-based Thermoplastics, Department of Chemistry and Chemical Engineering, Chalmers University of Technology, Gothenburg 412 96, Sweden;* orcid.org/0000-0001-8153-2129

    Elin Persson Jutemar − *Tetra Pak, Lund 221 86, Sweden;* orcid.org/0000-0002-9076-1385

    Renan Melhado Mazza − *Tetra Pak, Lund 221 86, Sweden;* orcid.org/0009-0002-8463-8062

    Eskil Andreasson − *Tetra Pak, Lund 221 86, Sweden;* orcid.org/0000-0001-8325-9226

    Fredrik Linell − *Tetra Pak, Lund 221 86, Sweden;* orcid.org/0009-0007-3817-9121

    Manuel Guizar-Sicairos − *Paul Scherrer Institute, Villigen 5232, Switzerland; Ecole Polytechnique Fédérale de Lausanne (EPFL), Lausanne 1015, Switzerland;* orcid.org/0000-0002-8293-3634

Complete contact information is available at:
https://pubs.acs.org/10.1021/acsapm.4c00581

■ ACKNOWLEDGMENTS

■ REFERENCES

(1) Angelloz, C.; Fulchiron, R.; Douillard, A.; Chabert, B.; Fillit, R.; Vautrin, A.; David, L. Crystallization of Isotactic Polypropylene under High Pressure (γ Phase). *Macromolecules* **2000**, *33* (11), 4138−4145.

(2) Pantani, R.; Coccorullo, I.; Speranza, V.; Titomanlio, G. Morphology evolution during injection molding: Effect of packing pressure. *Polymer* **2007**, *48* (9), 2778−2790.

(3) Wang, J.; Wang, L.; Bian, N.; Wang, D.; Wang, Y.; Zhang, Y.; Li, Q.; Shen, C. Influence of shear history on morphology, microstructure and mechanical properties of micro injection molded parts. *Huagong Xuebao/CIESC Journal* **2015**, *66*, 1931−1938.

(4) Boyer, S.A.E.; Haudin, J.-M. Crystallization of polymers at constant and high cooling rates: A new hot-stage microscopy set-up. *Polym. Test.* **2010**, *29* (4), 445−452.

(5) Zhao, X.; Liao, T.; Yang, X.; Coates, P.; Whiteside, B.; Barker, D.; Thompson, G.; Jiang, Z.; Men, Y. Mold temperature- and molar mass-dependent structural formation in micro-injection molding of isotactic polypropylene. *Polymer* **2022**, *248*, 124797.

(6) Wingstrand, S. L.; van Drongelen, M.; Mortensen, K.; Graham, R. S.; Huang, Q.; Hassager, O. Influence of Extensional Stress Overshoot on Crystallization of LDPE. *Macromolecules* **2017**, *50* (3), 1134−1140.

(7) Fernandez, E.; Edeleva, M.; Fiorio, R.; Cardon, L.; D'hooge, D. R. Increasing the Sustainability of the Hybrid Mold Technique through Combined Insert Polymeric Material and Additive Manufacturing Method Design. *Sustainability* **2022**, *14* (2), 877.

(8) Tan, V.; Kamal, M. R. Morphological Zones and Orientation in Injection-Molded Polyethylene. *J. Appl. Polym. Sci.* **1978**, *22*, 2341−2355.

(9) Pantani, R.; Coccorullo, I.; Speranza, V.; Titomanlio, G. Modeling of morphology evolution in the injection molding process of thermoplastic polymers. *Prog. Polym. Sci.* **2005**, *30* (12), 1185−1222.

(10) Rong Zheng, R. I. T.; Lee Wo, D.; Fan, X.; Hadinata, C.; Costa, F. S.; Kennedy, P. K.; Zhu, P.; Edward, G. Modeling of flow-induced crystallization of colored polypropylene in injection molding. *Korea-Australia Rheology Journal* **2010**, *22* (3), 1.

(11) Solanki, B.; Singh, H.; Sheorey, T. Modeling and analysis of cavity modification effect on quality of injection molded polymer gear. *International Journal on Interactive Design and Manufacturing (IJIDeM)* **2022**, *16*, 1615.

(12) Liu, X.; Zheng, G.; Jia, Z.; Li, S.; Liu, C.; Zhang, Y.; Shao, C.; Dai, K.; Liu, B.; Zhang, Q.; Wang, S.; Liu, C.; Chen, J.; Peng, X.; Shen, C. The hierarchical structure of water-assisted injection molded high density polyethylene: Small angle X-ray scattering study. *J. Appl. Polym. Sci.* **2012**, *125* (3), 2297−2303.

(13) Wang, L.; Wang, J. H.; Yang, B.; Wang, Y.; Zhang, Q. P.; Yang, M. B.; Feng, J. M. A novel hierarchical crystalline structure of injection-molded bars of linear polymer: co-existence of bending and normal shish-kebab structure. *Colloid Polym. Sci.* **2013**, *291* (6), 1503−1511.

(14) Bartczak, Z.; Vozniak, A. WAXS/SAXS study of plastic deformation instabilities and lamellae fragmentation in polyethylene. *Polymer* **2019**, *177*, 160−177.

(15) Schrauwen, B. A. G.; Janssen, R. P. M.; Govaert, L. E.; Meijer, H. E. H. Intrinsic Deformation Behavior of Semicrystalline Polymers. *Macromolecules* **2004**, *37* (16), 6069−6078.

(16) Schrauwen, B. A. G.; Breemen, L. C. A. v.; Spoelstra, A. B.; Govaert, L. E.; Peters, G. W. M.; Meijer, H. E. H. Structure, Deformation, and Failure of Flow-Oriented Semicrystalline Polymers. *Macromolecules* **2004**, *37* (23), 8618−8633.

(17) Padden, F. J.; Keith, H. D. Spherulitic Crystallization in Polypropylene. *J. Appl. Phys.* **1959**, *30* (10), 1479−1484.

(18) Keller, A.; Machin, M. J. Oriented crystallization in polymers. *Journal of Macromolecular Science, Part B* **1967**, *1* (1), 41−91.

(19) Björn, L.; Melhado Mazza, R.; Andreasson, E.; Linell, F.; Lutz-Bueno, V.; Guizar-Sicairos, M.; Persson Jutemar, E.; Liebi, M. Scanning Small-Angle X-ray Scattering of Injection-Molded Polymers: Anisotropic Structure and Mechanical Properties of Low-Density Polyethylene. *ACS Applied Polymer Materials* **2023**, *5* (8), 6429−6440.

(20) Nichols, S.; Freudenthal, J.; Arteaga, O.; Kahr, B. Imaging with photoelastic modulators. *SPIE Sensing Technology + Applications* **2014**, *9099*, 1.

(21) Han, C.-Y.; Chao, Y.-F. Photoelastic modulated imaging ellipsometry by stroboscopic illumination technique. *Rev. Sci. Instrum.* **2006**, *77* (2), 1.

(22) Henrich, B.; Bergamaschi, A.; Broennimann, C.; Dinapoli, R.; Eikenberry, E. F.; Johnson, I.; Kobas, M.; Kraft, P.; Mozzanica, A.; Schmitt, B. PILATUS: A single photon counting pixel detector for X-ray applications. *Nuclear Instruments and Methods in Physics Research Section A: Accelerators, Spectrometers, Detectors and Associated Equipment* **2009**, *607* (1), 247−249.

(23) Bunk, O; Bech, M; Jensen, T H; Binderup, T; Menzel, A; Pfeiffer, F Multimodal x-ray scatter imaging. *New J. Phys.* **2009**, *11*, 123016.

(24) Ferri, D.; Perolo, A.; Nodari, M. Cross-WLF parameters to predict rheological properties of polylactic acid. *Annual transactions of the Nordic rheology society* **2017**, *25*, 419−426.

(25) van Drongelen, M.; Cavallo, D.; Balzano, L.; Portale, G.; Vittorias, I.; Bras, W.; Alfonso, G. C.; Peters, G. Structure Development of Low-Density Polyethylenes During Film Blowing: A Real-Time Wide-Angle X-ray Diffraction Study. *Macromol. Mater. Eng.* **2014**, *299*, 1494.

(26) Katti, S. S.; Schultz, M. The Microstructure of Injection-Molded Semicrystalline Polymers: A Review. *Polymer Engineering and Science* **1982**, *22* (16), 1001.

(27) Pantani, R.; Speranza, V.; Titomanlio, G. Relevance of mold-induced thermal boundary conditions and cavity deformation in the simulation of injection molding. *Polym. Eng. Sci.* **2001**, *41* (11), 2022−2035.

(28) Mavridis, H.; Hrymak, A. N.; Vlachopoulos, J. The Effect of Fountain Flow on Molecular Orientation in Injection Molding. *J. Rheol.* **1988**, *32* (6), 639−663.

(29) Derakhshandeh, M.; Hatzikiriakos, S. Flow-induced crystallization of high-density polyethylene: The effects of shear and uniaxial extension. *Rheol. Acta* **2011**, *51* (4), 1.

(30) Somani, R. H.; Yang, L.; Zhu, L.; Hsiao, B. S. Flow-induced shish-kebab precursor structures in entangled polymer melts. *Polymer* **2005**, *46* (20), 8587−8623.

(31) Zhang, C.; Hu, H.; Wang, D.; Yan, S.; Han, C. C. In situ optical microscope study of the shear-induced crystallization of isotactic polypropylene. *Polymer* **2005**, *46* (19), 8157−8161.

(32) Keum, J. K.; Burger, C.; Zuo, F.; Hsiao, B. S. Probing nucleation and growth behavior of twisted kebabs from shish scaffold in sheared polyethylene melts by in situ X-ray studies. *Polymer* **2007**, *48* (15), 4511−4519.

(33) Zhang, X.-X.; Yang, S.-G.; Hua, W.-Q.; Lin, J.-M.; Lei, J.; Bian, F.-G.; Xu, L.; Li, Z.-M. Role of pressure in flow-induced shish-kabab in binary blend of long- and short-chain Polyethylenes. *POLYMER CRYSTALLIZATION* **2019**, *2* (3), e10059.

(34) Mykhaylyk, O. O.; Chambon, P.; Graham, R. S.; Fairclough, J. P. A.; Olmsted, P. D.; Ryan, A. J. The Specific Work of Flow as a Criterion for Orientation in Polymer Crystallization. *Macromolecules* **2008**, *41* (6), 1901−1904.

(35) Mykhaylyk, O. O.; Chambon, P.; Impradice, C.; Fairclough, J. P. A.; Terrill, N. J.; Ryan, A. J. Control of Structural Morphology in Shear-Induced Crystallization of Polymers. *Macromolecules* **2010**, *43* (5), 2389−2405.

(36) Meerveld, J.; Peters, G.; Hütter, M. Towards a rheological classification of flow induced crystallization experiments of polymer melts. *Rheol. Acta* **2004**, *44*, 119−134.

(37) Janeschitz-Kriegl, H.; Ratajski, E.; Stadlbauer, M. Flow as an effective promotor of nucleation in polymer melts: a quantitative evaluation. *Rheol. Acta* **2003**, *42* (4), 355−364.

(38) Liparoti, S.; Speranza, V.; Pantani, R.; Titomanlio, G. Process Induced Morphology Development of Isotactic Polypropylene on the Basis of Molecular Stretch and Mechanical Work Evolutions. *Materials (Basel)* **2019**, *12* (3), 505.

(39) Pantani, R.; Speranza, V.; Titomanlio, G. A Criterion for the Formation of Fibrillar Layers in Injection Molded Parts. *Int. Polym. Process.* **2018**, *33* (3), 355−362.

(40) Du, M.; Jariyavidyanont, K.; Boldt, R.; Tariq, M.; Fischer, M.; Spoerer, Y.; Kuehnert, I.; Androsch, R. Crystal-nuclei formation during injection-molding of poly (l-lactic acid). *Polymer* **2022**, *250*, 124897.

(41) Fulchiron, R.; Koscher, E.; Poutot, G.; Delaunay, D.; Regnier, G. Analysis of the pressure effect on the crystallization kinetics of polypropylene: Dilatometric measurements and thermal gradient modeling. *J. MACROMOL. SCI.—PHYSICS* **2007**, *B40* (3&4), 297−314.